Mechanistic Insights into NO_x Production in Microwave Plasma at Intermediate Pressure

Qinghao Shen,[†,‡] Lex Kuijpers,[†,‡] Jonas Gans,[†,‡] Serguei Starostine,[†] Vasco Guerra,[¶] and Mauritius C.M. van de Sanden[*,†,‡]

†*Dutch Institute for Fundamental Energy Research, Eindhoven, The Netherlands*

‡*Department of Applied Physics, Eindhoven Institute of Renewable Energy Systems, Eindhoven University of Technology, Eindhoven, The Netherlands*

¶*Instituto de Plasmas e Fusão Nuclear, Instituto Superior Técnico, Universidade de Lisboa, Lisboa, Portugal*

E-mail: m.c.m.v.d.sanden@tue.nl

Abstract

Microwave plasma has emerged as one of the most energy-efficient approaches for nitrogen fixation. To elucidate the underlying mechanisms at intermediate pressure, a quasi-1.5D physico-chemical multi-temperature model is developed under varying N_2–O_2 compositions. The plasma shape and radial gas temperature profile, derived from the emission intensity distribution and the Doppler broadening of the 777 nm $O(^5S \leftarrow ^5P)$ atomic oxygen triplet, serve as key model inputs for determining the power density profile and turbulent viscosity, respectively. The model captures the coupled interplay among vibrational, chemical, and electron kinetics in microwave plasma NO_x synthesis, with particular emphasis on the role of vibrational excitation at 80 mbar. The energy costs predicted by the model show good agreement with the experimental results measured using Fourier-transform infrared spectroscopy. Non-thermal behavior

within the plasma core is found to strongly promote NO formation. Radial diffusion emerges as a key mechanism for sustaining chemical non-equilibrium, and improving overall NO yield. Key reactions involved in NO formation and destruction under different initial gas mixtures are discussed. Finally, it is suggested that the energy cost can be improved by optimizing the plasma shape. This work offers fundamental insights into the underlying plasma–chemical mechanisms and establishes a predictive framework to guide the future design and optimization of energy-efficient microwave plasma technologies for nitrogen fixation.

Keywords: non-thermal behavior, NO_x synthesis, microwave plasma, energy cost, vibrational enhancement, plasma modeling.

Introduction

Sustainability has gained growing significance in the chemical manufacturing sector due to global environmental and energy challenges.[1] The environmental burden imposed by industrial operations demands immediate mitigation efforts.[2] A prominent example is nitrogen fixation via the traditional Haber–Bosch (H–B) process.[3,4] Due to its relatively low energy requirement (0.48 MJ mol^{-1} for ammonia synthesis), the H–B process has been the dominant method for industrial nitrogen fixation (NF) for decades. However, the process remains heavily dependent on fossil fuels, lacks flexibility, and achieves optimal energy efficiency only at large scales.[5–7] Given that the current H–B process has nearly reached its technological limits, further improvements through process optimisation are constrained.[8]

The advent of low-cost, intermittent renewable electricity may fundamentally reshape technology preferences in NF.[9] Electrification-driven chemical conversion has emerged as a pivotal technology for advancing renewable energy integration and achieving carbon neutrality.[10,11] From an environmental perspective, plasma-assisted NF is potentially promising, as it enables direct conversion of abundant N_2-O_2 mixtures into value-added products using solely electrical energy.[12–15] When powered by renewable energy, this approach could enable

fertilizer production with near-zero greenhouse gas emissions, given that plasma processes generate minimal waste and require no special solvents.[8]

In recent years, a substantial body of experimental research has emerged in the field of plasma-based nitrogen fixation, as is shown in Figure 1. Dielectric barrier discharge (DBD) plasma, as a typical example of cold plasma, has a simple design, making it easy for upscaling and commercial applications.[13] However, DBD plasmas exhibit low energy efficiency, as the electron energy is typically too high for optimal gas dissociation. Compared to cold plasmas, warm plasmas, such as microwave (MW) and gliding arc (GA) plasmas, have demonstrated significantly lower energy cost for NO_x synthesis.[16] A critical challenge persists: while plasma-based nitrogen fixation can achieve competitive efficiency levels in theory (0.2 MJ(mol N)$^{-1}$), its current lowest experimental energy costs remain prohibitively high (1.708 MJ(mol N)$^{-1}$),[17] rendering the technology economically unviable at present.[18,19] If the energy consumption can be reduced to 1.0–1.5 MJ(mol N)$^{-1}$, plasma-based NO_x synthesis has the potential to emerge as a highly competitive alternative to the conventional Haber–Bosch and Ostwald processes.[9,20]

In order to improve the reactor design for better performance, modeling usually allows for trying many different possibilities in a much easier and less costly way than by performing the corresponding experiments.[9,18] Zero-dimensional (0D) chemical kinetic models are extensively used for elucidating the fundamental plasma-chemical reaction pathways governing the dynamics of NO_x synthesis, as they enable efficient simulation of extensive reaction networks involving numerous species while maintaining manageable computational demands.[61,62] Shuai *et al.* have employed a 0D chemical kinetics model to reveal that over 50% of NO is generated from vibrational Zeldovich reactions in a nanosecond repetitive pulse air spark discharge at ambient conditions.[54] The model assumes identical rate coefficients for Zeldovich reactions across all vibrational levels, consequently underestimating the enhanced contribution of highly vibrationally excited states to NO formation. In another 0D chemical kinetics model, Vervloessem *et al.* have scaled the rate coefficients of Zeldovich

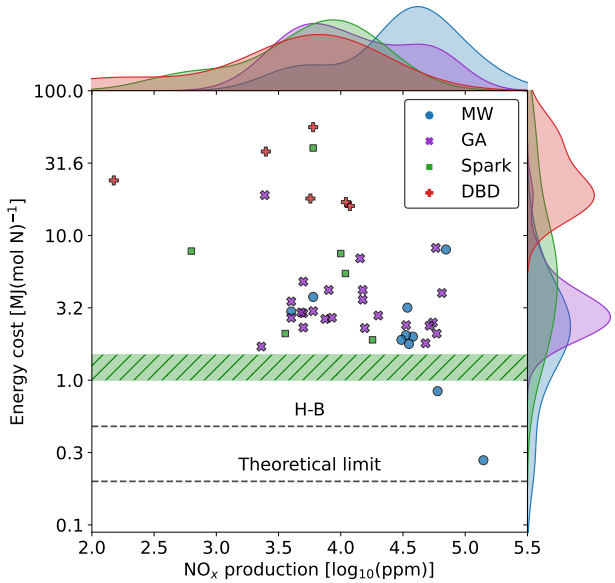

Figure 1: Experimental data collected from the literature for NF using different discharges, showing the energy cost as a function of the NO_x yield. Each data point represents the optimal experimental conditions reported in different studies. GA represents Gliding Arc discharge;[17,21–41] MW represents Microwave discharge;[42–51] Spark represents spark discharge;[52–57] DBD represents Dielectric Barrier Discharge.[22,53,55,58–60] The marginal density plots (located at the top and right) illustrate the distribution of data points along each axis. The green-highlighted area represents the techno-economic target that must be surpassed to achieve industrial viability.[9,20]

reactions at different vibrational states based on the Fridman-Macheret approach.[41] However, Esposito has critically noted that the Fridman-Macheret approach is inadequate for obtaining accurate Zeldovich reaction rate coefficients, particularly at high vibrational levels.[18] More recently, Esposito and Armenise computed the rate coefficients of two Zeldovich reactions across various vibrational levels and a broad range of gas temperatures using the quasi-classical trajectory (QCT) method, yielding more precise results for future modeling efforts.[63–65]

Altin *et al.* have established a 1D fluid radial model to elucidate the generation mechanisms of vibrationally excited N_2 in pulsed MW discharges in pure N_2 at moderate pressure.[66] In our previous work, a 1D axial multi-temperature model has been implemented to investigate NO_x formation and destruction pathways in the downstream region of MW air plasmas, revealing that vibrational excitation exhibits limited influence on NO produc-

tion in atmospheric-pressure afterglows.[67] Based on three quasi-one-dimensional (quasi-1D) models, representing different areas of the reactor in the radial direction, Kelly *et al.* have demonstrated that elevated inflow rates simultaneously enhance forward reactions in the Zeldovich mechanism while suppressing reverse reactions within the plasma region.[46] However, particle diffusion is neglected in the model. This may alter the thermophysical properties of the gas mixture, such as enthalpy and thermal conductivity, potentially leading to inaccurate results.[68,69] This limitation has been addressed by the quasi-1.5D model of our previous research.[70] The model successfully reproduces the pronounced non-thermal behaviour of N_2 in the plasma region at 80 mbar, although this non-equilibrium state diminishes rapidly in the afterglow.

To the best of our knowledge, comprehensive two- or three-dimensional (2D or 3D) models for gas conversion processes remain rare. Majeed *et al.* have implemented a 3D thermal-turbulent model to examine quenching processes with varying gas ratios in atmospheric-pressure rotating arc plasmas.[31] Van Alphen *et al.* have developed another 3D thermal-turbulent model to evaluate the impact of an effusion nozzle downstream of a rotating gliding arc plasma reactor.[28] Both of the above studies treat plasma solely as a heat source, neglecting electron, vibrational, and even chemical kinetics.[28,31] This limitation primarily stems from computational constraints, as incorporating detailed plasma chemistry in higher-dimensional models currently leads to prohibitively long calculation times.[61] Recently, Tatar *et al.* have established a 3D thermal-laminar model, successfully incorporating simplified neutral-species chemistry for microwave air plasmas at 650 mbar.[71] Their findings have indicated that NO formation predominantly occurs in the peripheral plasma regions at this pressure, as the extreme temperatures in the core significantly exceed the optimal range for NO synthesis. While experimental studies have confirmed the thermal equilibrium between gas and vibrational temperatures at high pressures,[71] supporting the validity of the thermal plasma assumption, this approximation becomes inadequate at low to intermediate pressures, where vibrational excitation significantly impacts NO production.[44] Hence, the prior

assumption that plasma functions solely as a heat source may lead to an underestimation of NO production under low to intermediate pressure conditions.

In this context, the present work aims to investigate the coupled interplay among vibrational, chemical, and electron kinetics, thermodynamic processes, and transport phenomena across both the discharge and afterglow phases. Particular emphasis is placed on elucidating the fundamental reaction mechanisms governing NO formation and destruction under varying initial gas compositions. This study offers key insights into the role of vibrational kinetics in enhancing NO production at intermediate pressures. Furthermore, several computational optimisation strategies are proposed to reduce numerical cost, laying a critical foundation for future high-dimensional modeling. While the present study does not extend to plasma-assisted NH_3 synthesis, the insights gained—particularly regarding plasma activation of N_2, radical generation, and product selectivity—are directly relevant to broader nitrogen fixation strategies. Therefore, the approach developed here may serve as a foundation for future innovations, including extensions toward plasma-driven NH_3 synthesis.

Experimental setup and results

The plasma reactor features a 27 mm internal diameter quartz glass tube mounted within a WR340 waveguide, driven by a microwave power source operating at 2.45 GHz. The reactor configuration builds upon our previous designs, with additional details available in prior publications.[72] Experiments were conducted, using N_2-O_2 (purity of 99.999%) mixtures at varied mixing ratios, with total flow rates maintained at 10 standard liters per minute (slm) and the reactor pressure fixed at 80 mbar. The possible influence of trace impurities or minor species in the feed gas on plasma chemistry was not considered in this study and may represent a limitation that warrants further investigation. A constant microwave power of 800 W was applied for all conditions. The 800 W setting was chosen as a balanced and judicious operating point under the specific conditions of 80 mbar pressure and a 10 slm

flow rate. It was observed that below this threshold, variations in discharge power exerted only a minor influence on the energy cost of NO_x production. However, when the applied power exceeded 800 W, the plasma volume expanded significantly and extended toward the quartz tube wall. Such expansion poses a substantial risk of thermal stress or even melting of the quartz containment, thereby defining 800 W as the practical upper operational limit. The NO_x products were generated in the gas phase and collected from the reactor outlet through a gas sampling line. Their concentrations were quantified using Fourier-transform infrared (FTIR) spectroscopy, which enabled simultaneous and selective detection of NO_x species. The FTIR measurements were conducted using a 50 cm absorption cell maintained at 50 mbar. To accurately determine the gas concentrations, the acquired spectra were processed by a Levenberg–Marquardt least-squares fitting algorithm. This procedure minimized the discrepancy between the experimental data and theoretical spectra derived from the comprehensive HITRAN database.[73] The distinct absorption regions allowed for clear separation of the target species: NO was identified by its characteristic features in the $\sim$1740–1990 cm^{-1} range, while NO_2 exhibited strong absorption between $\sim$1500–1700 cm^{-1}. Furthermore, N_2O, N_2O_3, N_2O_4, and N_2O_5 were only present at trace concentration levels, which is consistent with previous studies.[17,41,46] A representative example of the excellent agreement achieved between the measured and fitted spectra is shown in the figure provided in the supporting material.

Figure 2 shows the calculated and measured radial temperature profiles with different gas ratios of N_2. The good agreement between the calculated and measured data provides confidence in the modeling. The experimental gas temperature profiles are determined through Doppler broadening measurements of the 777 nm O(^{5}S$\leftarrow$^{5}P) oxygen triplet emission, employing a similar methodology to our previous CO_2 plasma characterization.[74] The high-resolution spectrometer enabled independent fitting of all three triplet peaks, the reported temperatures representing the average of these measurements. Discharge dimensions were characterized using the full-width at e^{-2} ($\approx$13.5%) of the 777 nm oxygen triplet emission

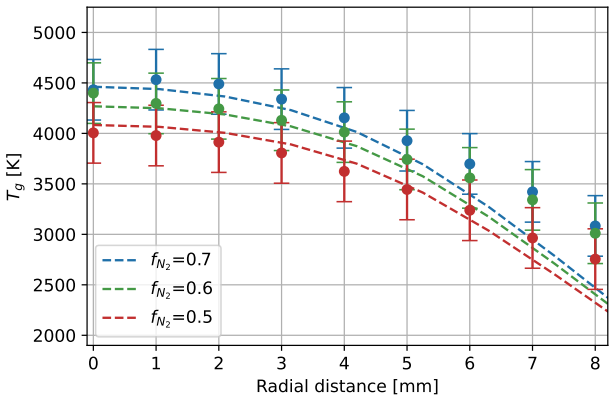

Figure 2: Radial profiles of the maximum gas temperature at various N_2 fraction f_{N_2}. Dashed lines represent simulation results, while dots correspond to experimental data.

intensity profile, captured by a CCD sensor equipped with a 780 nm bandpass filter.[74] Radial intensity profiles were reconstructed via discrete inverse Abel transformation using the Hansen and Law algorithm.[72] Given the observed radial homogeneity of discharge emission at low pressures, a Super-Gaussian distribution was implemented to fit the plasma radius R_{dis} [in mm]. The exponent values n, which determine the shape of the Super-Gaussian distribution, are presented in Table 1 for different conditions. When n equals 2, the Super-Gaussian distribution becomes the standard Gaussian distribution. The plasma length L_{dis} [in mm] is calculated by fitting a Gaussian distribution directly. The energy cost EC [in MJ (mol N)$^{-1}$] is calculated by:

$$\mathrm{EC} = \frac{P_{total}}{C_{total} X_{NO_x}} \times 10^{-6} \tag{1}$$

where P_{total} [in W] is the total input power, C_{total} [in mol s^{-1}] is the molar flow rate for output, X_{NO_x} is the molar fraction of NO_x [in %]. All the experimental data can be found in Table 1, which are also used as inputs to the simulations or for validation.

Table 1: Experimental results under different conditions.

f_{N2} [-]	R_{dis} [mm]	L_{dis} [mm]	n	EC [MJ (mol N)$^{-1}$]	X_{NO} [%]	X_{NO_2}[%]
0.5	8.4	40	6.4	3.31±0.19	3.23±0.14	0.05±2.17E-3
0.6	8.4	40	5.8	3.23±0.18	3.33±0.14	0.04±1.62E-3
0.7	8.3	42	5.6	3.29±0.19	3.33±0.14	0.03±1.24E-3
0.8	8.3	44	7.4	3.52±0.20	3.31±0.13	0.02±8.01E-4
0.9	8.5	47	5.2	4.89±0.27	2.22±0.10	0.01± 3.21E-4

Modeling

In plasma-assisted NF, particularly at low or intermediate pressures, the system is characterised by strong non-equilibrium features, where electrons, heavy particles, and vibrationally excited molecules exist at different temperatures. There are complex and interdependent dynamics among electron, vibrational, and chemical kinetics.[75] Electrons gain relatively high mean energies (typically in the range of 1–3 eV for MW plasma[46]) from externally applied electric fields, which far exceed the thermal energies of the heavy species. These energetic electrons are the primary drivers of non-equilibrium excitation processes, including vibrational and electronic excitation, ionisation, and dissociation.[75] Vibrational energy is capable of accelerating chemical reaction rates by effectively lowering the activation energy barrier of chemical reactions (mostly Zeldovich reactions in the NF process).[29] Additionally, vibrational-translational (V–T) relaxation processes can also accelerate endothermic reactions by affecting gas temperature. In turn, the gas composition, which is changed by various chemical processes, can affect the electron energy distribution function (EEDF), and the electron kinetics.[76] Thus, the interplay between electron, vibrational, and chemical kinetics constitutes a non-linearly coupled system, where small changes in one domain can cascade across the others.

To elucidate the underlying mechanisms of the MW plasma-assisted NO_x synthesis in the above-mentioned experimental conditions, a generalised multi-temperature (MT) quasi-1.5D 'physico-chemical' model is introduced, which is based on our previous work[70]. In the MT model, characteristic vibrational temperatures are obtained by equating the total vibrational

energy to that of a Boltzmann distribution at a specific temperature, effectively capturing the average vibrational excitation under non-equilibrium conditions.[70] This coarse-grained description significantly reduces the complexity of the system.[77] More detailed information on the governing equations of the MT method can be found in our previous work.[67,70] These efforts lay the groundwork for future integration with multi-dimensional computational fluid dynamics (CFD) solvers, thereby enabling more comprehensive and efficient modeling of plasma-assisted gas conversion processes at the reactor scale.

The model simulates the entire process domain, including both the discharge (within the plasma length) and its afterglow. In the radial direction, the domain is divided into two regions: the central region (within the plasma radius) and the outer region. The central region in the discharge is defined as the plasma region. Each of these regions is discretised into a series of concentric cylindrical volume elements, which are represented by individual 1D axial plug flow reactors (PFRs).[70]

The 1D PFR model with a fixed length is represented by a series of 0D continuous stirred tank reactors (CSTRs).[78] To balance computational cost and accuracy, an adaptive grid method is employed:[67] the length of each CSTR in the PFR model is variable and determined based on local temperature gradients. Specifically, if the temperature difference, whether in gas or vibrational temperature, between two consecutive CSTRs along the axial direction is less than 2 K, the model recalculates the current step with a longer CSTR length to avoid computational redundancy. Conversely, if the temperature difference exceeds 10 K, the model recalculates the step with a shorter CSTR length to preserve accuracy. In this way, the current methods are able to reduce computational cost while maintaining accuracy.

In this work, there are three primary improvements compared to our previous 1.5D model.[70] Firstly, the assumption of non-equilibrium vibrational behaviour is extended beyond the plasma to include the outer region. Therefore, possible vibrationally enhanced NO formation in the outer region can be included. Secondly, because previous studies have shown that the vibrational temperature of O_2 remains close to the gas (translation-rotational)

temperature, O_2 is treated as fully thermalised in this work to reduce unnecessary computational cost. The impact of this simplification is briefly discussed in the supporting material. Lastly, the current model employs more PFRs to simulate the central region and outer regions, respectively. Compared to the previous configuration, which used a single PFR for the central and three for the outer region,[70] this refined setup enables better resolution of radial gradients in temperature and species composition, thereby improving the accuracy of the simulation results. The influence of the PFR number in both regions on the simulation outcomes is further analysed in the supporting material.

The vibrational levels and vibrational energies for the ground state of N_2, as reported by Esposito *et al.*,[65] are provided in our previous work.[67,70] Table 2 summarizes all vibrational excitation and relaxation processes considered in the model. Vibrational-vibrational (V-V) N_2–N_2 collisions are excluded due to their negligible contribution to vibrational energy loss and disproportionately high computational cost.[70] Since O_2 is assumed to be fully thermalised, all vibrational energy transferred from N_2 to O_2 via V-V N_2-O_2 relaxation is directly converted into gas heating, and the vibrational level population of O_2 is set based on the gas temperature. A more detailed description of the methods used to calculate rate coefficients, including the forced harmonic oscillator (FHO), mixed quantum-classical (MQC), and generalized Fridman–Macheret (GFM) approaches, can be found in our previous studies.[67,70,79] The electron kinetics is computed using the LisbOn KInetics Boltzmann solver(LoKI-B), which provides a detailed, self-consistent solution of the electron energy distribution function (EEDF) under non-equilibrium conditions.[80,81] All the electron impact collisions and chemical reactions taken into account in this model can be found in the supporting material of our previous work.[70] The model is implemented using Cantera, an open-source Python library for chemical kinetics, thermodynamics, and transport simulations.[82] All species included in the model are listed in Table 3. Additionally, the governing equations are presented in detail in our previous work.[67,70]

The initial gas temperature in the center is set to 2000 K, and the radial gas tempera-

Table 2: List of vibrational state-specific kinetic mechanisms. i and i^* are lower than 60, and not equal. j is lower than 46.

Type	Process	Method	Ref
V-T	$N_2(i)+N_2 \leftrightarrow N_2(i^*)+N_2$	FHO	[83]
V-T	$N_2(i)+O_2 \leftrightarrow N_2(i^*)+O_2$	FHO	[83]
V-T	$N_2(i)+N \leftrightarrow N_2(i^*)+N$,	QCT	[84,85]
V-T	$N_2(i)+O \leftrightarrow N_2(i\text{-}1)+O$ ($i \leq 10$)	MQC	[86]
V-V	$N_2(i)+O_2(j) \leftrightarrow N_2(i+1)+O_2(j\text{-}1)$	FHO	[83]
Z-E	$N_2(i)+O \rightarrow NO+N$	MD	[63,65]
V-D	$N_2(i)+M \rightarrow N+N+M$ (M=N_2,N)	QCT	[84]
V-D	$N_2(i)+M \rightarrow N+N+M$ (M=O_2/O/NO/NO_2)	GMF	[67]

ture profile at the beginning is followed by the Super-Gaussian distribution until 300 K at the outermost region. Except for the power used for initial gas heating, all the remaining microwave power is assumed to dissipate in the plasma region. The power density profile in the model is determined by the plasma width and height from the experiments, based on Super-Gaussian and Gaussian distributions in the radial and axial direction, respectively, given by:

$$Q_{abs}(z,r) = Q_{abs}^{max} \exp\left[-\alpha_z \left(z - \frac{L_{dis}}{2}\right)^2\right] \exp\left(-\alpha_r r^n\right) \tag{2}$$

where $Q_{abs}(z,r)$ and Q_{abs}^{max} [both in W m^3] are power density and the peak power density, respectively; z and r [both in m] represent the axial and radial position within the plasma region, respectively; the parameters α_z and α_r are calculated by:

$$\exp\left[-\alpha_z \left(\frac{L_{dis}}{2}\right)^2\right] = \exp\left(-\alpha_r (R_{dis})^n\right) = e^{-2} \tag{3}$$

where the values of n, L_{dis} and R_{dis} can be found in Table 1. The peak power density Q_{abs}^{max} is calculated by ensuring that the integral of $Q_{abs}(z)$ over the computational volume is equal to the total power input, subtracting the energy required to heat the gas to the initial temperature.[87] As an example, Figure 3 illustrates the power density distribution in the plasma region under 50% N_2 fraction condition.

In our model, the enhancement of radial diffusion and thermal conductivity due to tur-

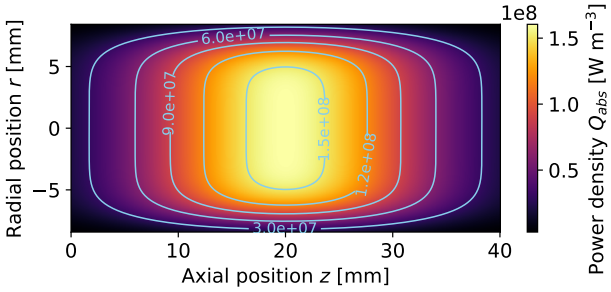

Figure 3: Power density distribution in the cross-sectional plane in the plasma region at 50% N_2 fraction.

Table 3: Chemical species included in this work.

Charged species	N^+, N_2^+, O^+, O_2^+, NO^+, NO_2^+, O^-, O_2^-, NO^-, e
Ground states	O, O_2, N, N_2, NO, NO_2,
Electronic states	$N(^2D)$, $N(^2P)$, $O(^1D)$, $O(^1S)$, $N_2(A\ ^3\Sigma_u^+)$, $N_2(B\ ^3\Pi_g)$ $N_2(C\ ^3\Pi_u)$, $N_2(a\ ^1\Pi_g)$, $O_2(a\ ^1\Delta_g)$, $O_2(b\ ^1\Sigma_g^+)$, $O_2(*)$

Note: $O_2(*)$ is a combination of three states, including $O_2(A\ ^3\Sigma_u^+, C\ ^3\Delta_u, c\ ^1\Sigma_u^-)$ at a threshold energy of 4.5 eV.

bulence is accounted for via the introduction of peak turbulent viscosity.[88,89] Based on CFD simulations of the vortex flow incorporating a plasma-representative heat source, the turbulent viscosity is found to follow a quadratic profile in the radial direction.[74] A limitation of the current model is that the maximum gas temperature does not occur at the axial centre of the plasma region, as might be expected from experimental observations. This discrepancy may arise from the assumption of a uniform turbulent viscosity along the axial direction, which neglects potential axial variations in turbulence intensity. Here, the value of peak turbulent viscosity is determined iteratively by matching the modelled radial gas temperature profile with the highest gas temperature to the experimental gas temperature profile in the centre of the plasma discharge, as is shown in Figure 2. It should be noted that coupling the Navier–Stokes (NS) equations with the current model to derive peak turbulent viscosity more accurately remains a critical next step. Based on the calculations, it is found that the peak turbulent viscosity is not sensitive to the gas composition. More detailed information about how to calculate the effective thermal conductivity and particle diffusion coefficients, including laminar and turbulence effects, is found in our previous work.[67,70]

Results and discussion

Temperature and species distribution

In this section, the case of the initial gas mixture with 50% N_2 content is used as an example to analyse the spatial distributions of temperatures and NO molar fraction. The gas and vibrational temperature profiles in the cross-sectional plane are shown in Figure 4. Since all the vibrational energy of N_2 originates from electron energy transfer,[70] the vibrational temperature distribution within the plasma (central discharge) region closely follows the power density profile. The peak vibrational temperature reaches 6142 K near the plasma core, where the power density is the highest. In the afterglow region, due to the absence of continuous electron energy input, the vibrational temperature drops rapidly. As a result, non-thermal behaviour decays quickly, which is consistent with previous findings.[70] Regarding gas temperature, only a very limited portion of the electron energy is directly used for gas heating via elastic collision or rotational excitation (see next subsection). The majority of the thermal energy originates from the quenching of electronically excited species or vibrational relaxation. Consequently, the gas temperature profile exhibits a delayed response relative to the power density distribution.

Compared with the plasma core, significant radial temperature gradients are observed in the surrounding plasma region. Stronger non-thermal behavior, characterized by a vibrational temperature exceeding the gas temperature by more than 1000 K, is primarily confined to the plasma region. Although the vibrational temperatures remain higher than the gas temperatures in the outer region, both temperatures are relatively low (less than 3000 K), rendering this area negligible in terms of NO production. Therefore, thermal equilibrium in the outer region can be reasonably assumed to reduce computational costs in future simulations.

Tatar *et al.* have demonstrated that NO formation primarily occurs at the plasma edge in MW air discharges at 650 mbar.[71] Similarly, Van Poyer *et al.* have reported that CO pro-

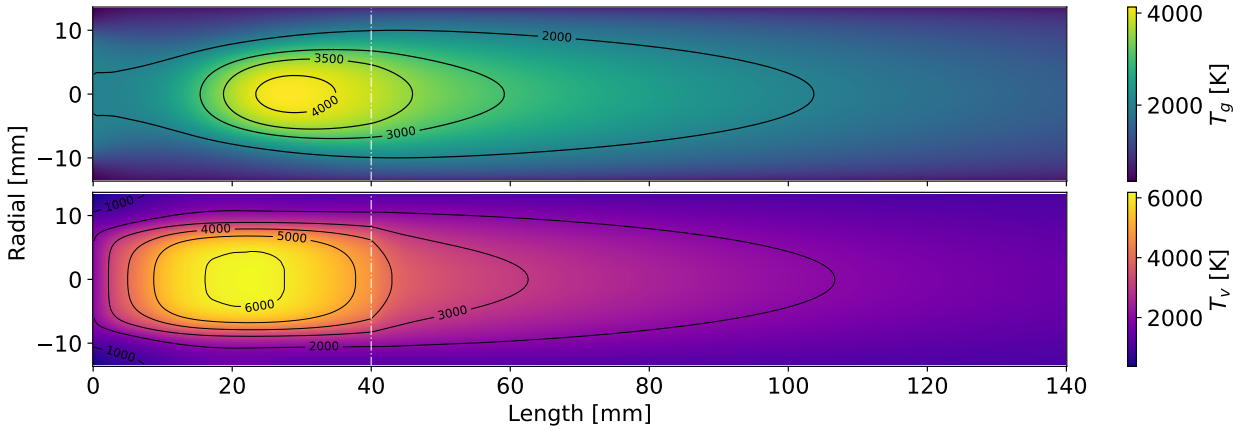

Figure 4: Gas and vibrational temperatures distribution in the cross-sectional plane in the middle of the reactor at 50% N_2 fraction. The white dashed line indicates the boundary between discharge and afterglow.

duction predominantly takes place at the plasma edge in CO_2 MW discharges at atmospheric pressure.[68] To investigate whether NO formation also concentrates at the plasma edge under intermediate pressure conditions, Figure 5 presents the spatial distribution of the NO molar fraction X_{NO} and its net production rate R_{NO}^{net} across the discharge and afterglow regions. At 80 mbar, the main NO formation zone is located in the plasma core rather than at the edge. This is attributed to the relatively moderate temperatures in the core (below 4200 K), which favour forward Zeldovich reactions while suppressing NO dissociation. In contrast, the plasma contraction at high pressures[72] leads to significantly elevated gas temperatures in the plasma core (exceeding 6000 K), in turn accelerating NO destruction in the plasma core.[71]

Although the vibrational temperature exceeds 4000 K (even reaching 5500 K of the boundary between the plasma and the afterglow), only a limited amount of NO (below 1%) is formed within the first 1.5 cm of the plasma region. This limited formation is primarily due to the relatively short residence time, which plays a critical role at low and intermediate pressures. As illustrated in Figure 6, the residence time under thermal conditions significantly influences the NO production, especially at low gas temperatures. Given that the residence time at 80 mbar is on the order of 0.1 ms,[74] even if elevated vibrational tempera-

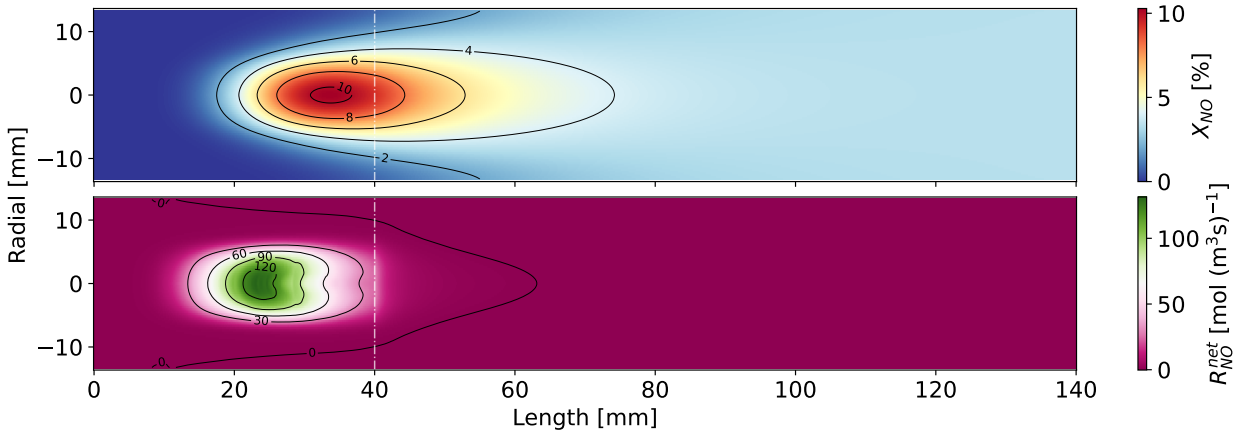

Figure 5: NO molar fraction and net production rate distribution in the cross-sectional plane in the middle of the reactor at 50% N_2 fraction. The net NO production rate is the sum of all the net rates of all reactions related to NO production (positive) and NO destruction (negative). The white dashed line indicates the boundary between discharge and afterglow.

tures can accelerate the reaction rates, and thereby reduce the chemical-equilibrium time,[79] such a short residence time can not effectively trigger NO formation in the first 1.5 cm of the plasma region.

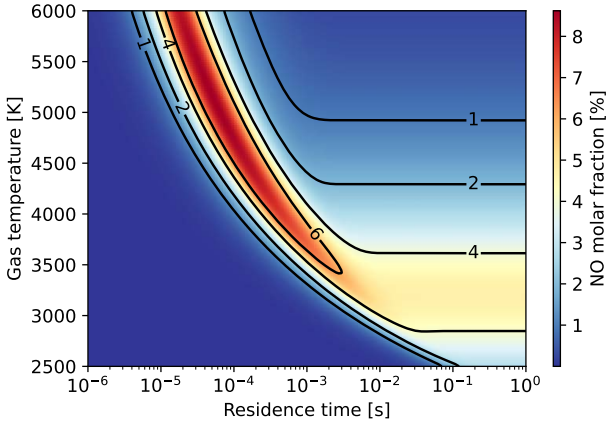

Figure 6: NO molar fraction as a function of residence time and gas temperature under thermal equilibrium conditions at 80 mbar for a 50% N_2–50% O_2 gas mixture.

As both vibrational and gas temperatures increase, NO formation intensifies in the second half of the plasma region, reaching a maximum molar fraction of 10.3%. In comparison, under thermal equilibrium (*i.e.*, T_g=T_v) conditions, the peak NO molar fraction is only 8.6%, revealing that N_2 vibrational excitation significantly enhances NO production at 80

mbar. The net NO production rate decreases rapidly at the onset of the afterglow and even becomes negative after the mid-afterglow region. However, this destructive effect is still very limited because the relatively low temperatures (both gas and vibrational temperatures are below 3000 K) inhibit the backward Zeldovich reactions and NO dissociation processes. Moreover, since the net NO production rate outside the plasma region is nearly zero, the NO present in the outer region is governed by diffusional transport from the center region to the outer region rather than chemical reactions. As a result, the NO molar fraction stabilises at approximately 3.36% across the entire radial direction by the end. Similarly, N and O atoms also diffuse radially from the central to the outer region due to concentration gradients (Figure S3 in the supporting material). Because the self-recombination rates of O and N atoms greatly exceed those of the forward and reverse Zeldovich reactions at low gas temperatures (below 2500 K), nearly all diffused N and O atoms recombine with themselves rather than participate in NO formation. This leads to an almost zero net NO production rate in the outer region.

Underlying mechanism of energy transfer and NO synthesis

Based on previous studies, it is well established that gas composition can significantly impact the distribution of electron energy among various channels, such as excitation, ionization, and dissociation.[70,76] Therefore, the fraction of total electron energy transferred to these channels under different initial gas compositions across the entire plasma region is investigated, and it is shown in Figure 7. Less than 1% of the electron energy is directly converted to gas heating through elastic and rotational collisions, and this value remains relatively insensitive to the N_2 fraction. Although more electron energy is transferred to the vibrational energy of O_2 with O_2 fraction increasing, the contribution remains negligible (approximately 1.5% at maximum). Consequently, it is reasonable to assume that O_2 is fully thermalised to reduce computational cost without compromising accuracy.

Due to the lower electronic excitation threshold of O_2 compared to N_2, more electron

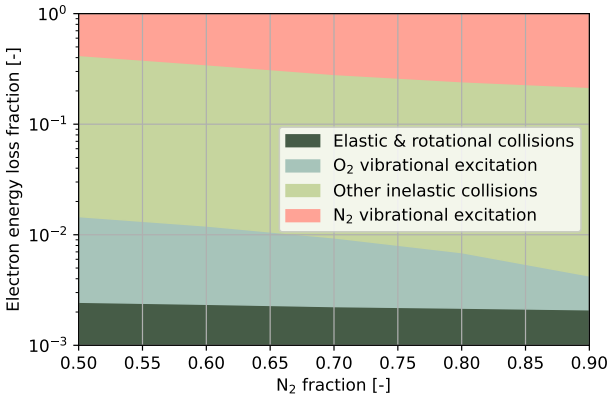

Figure 7: Cumulative fractions of electron energy transferred to different channels of elastic collision, rotational excitation, vibrational excitation of N_2 and O_2, and other inelastic collisions, including electronic excitation, dissociation, and ionization, in the whole plasma region as a function of N_2 fractions.

energy is directed toward O_2 electronic excitation at low N_2 fractions. As the N_2 fraction increases, a larger portion of the electron energy is redirected toward the vibrational excitation of N_2. Although over 60% of the electron energy is used for the vibrational excitation of N_2 across different N_2 fractions, most of this vibrational energy is not utilised to drive the forward Zeldovich reactions. Instead, it is dissipated as heat through various relaxation processes. Figure 8 illustrates the impact of different vibrational relaxation mechanisms at varying N_2 fractions. Compared with other relaxation processes, V-T N_2-O relaxation consistently accounts for the highest vibrational energy loss, particularly at high N_2 fractions. Due to the limited concentration of N atoms (Figure S1 in the supporting material), the energy loss via V–T N_2-N process is negligible (maximum value of 0.1% at 90% N_2 faction), despite its high relaxation rate coefficients.[67] As the N_2 fraction increases, the vibrational energy loss through V-V N_2–O_2 collisions decreases continually, with more vibrational energy instead being dissipated via V-T N_2–N_2 process.

The experimental energy cost and NO_x yields as a function of N_2 content are summarized in Table 1. Under all investigated conditions, the molar fraction of NO_2 remains very small compared to that of NO, confirming that NO is the dominant product in our experiments. This can be attributed to the strong temperature dependence of NO_2, which is primarily

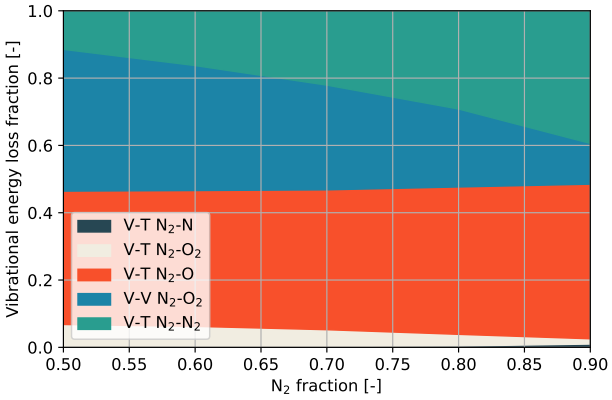

Figure 8: Cumulative fractions of vibrational energy losses in different relaxation processes in the whole process, including discharge and afterglow regions, as a function of N_2 fractions.

formed through the reaction $2NO + O_2 \rightarrow 2NO_2$ during the after-quenching stage, where the gas temperature is relatively low. A more detailed discussion on this aspect is provided in our previous work.[70] Although increasing the O_2 concentration enhances the reaction rate of NO_2 formation, the concentration of NO still remains significantly higher than that of NO_2 at intermediate pressure. When the N_2 content decreases from 90% to 70%, the energy cost drops by over 30%. The minimum energy cost is observed at a 60% N_2 fraction. This trend aligns with the findings from another MW discharge study conducted under comparable power at atmospheric pressure.[46] This behaviour can be attributed to the addition of O_2, which promotes the forward Zeldovich reactions. A more detailed discussion of these reaction pathways is presented in Figure 10. To investigate the effect of particle diffusion on NO_x production, the energy costs predicted by two non-thermal models, with and without particle diffusion, are compared in Figure 9. The model that includes particle diffusion shows good agreement with the experimental data across different N_2 fractions, highlighting the importance of transport processes in accurately capturing NO_x formation. This improvement is primarily attributed to the radial diffusion of NO molecules, which are formed in the high-temperature central region and gradually migrate outward due to concentration gradients. This outward transport lowers the local NO concentration in the plasma core, thereby suppressing the reverse Zeldovich and NO dissociation reactions as a result of reduced re-

actant availability. Consequently, diffusion helps to prolong the chemical non-equilibrium conditions in the core region. As shown in Figure 9, when diffusion is excluded, the predicted energy costs deviate significantly from experimental measurements. Therefore, accurately modeling diffusion is essential for predicting both NO formation and its spatial distribution. Moreover, as the N_2 fraction increases, the gas temperature in the plasma core can exceed 5000 K (at 90% N_2 fraction). Higher temperatures accelerate the reverse Zeldovich reactions and enhance NO dissociation, promoting faster chemical equilibration and further reducing NO yields in the absence of diffusion. Therefore, the discrepancy in energy cost between models with and without diffusion becomes even more pronounced.

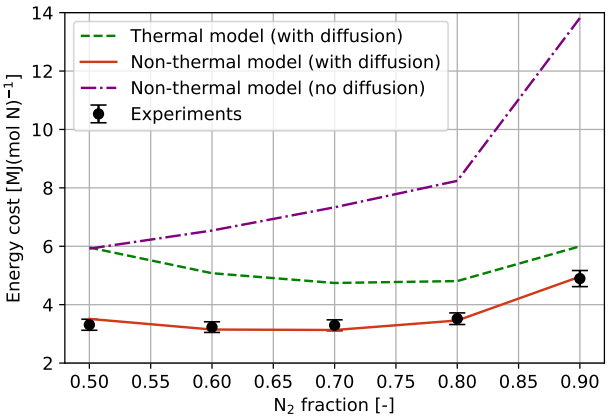

Figure 9: Experimental (dots) and calculated (lines) energy cost as a function of N_2 fraction in the different models.

In order to assess the enhancement of NO_x production due to vibrational non-equilibrium, a thermal model is employed as a baseline, in which the electron energy is assumed to be equally distributed across all molecular modes.[70] Therefore, the vibrational temperatures are always equal to the gas temperatures in the thermal model. It is evident that the thermal model results show considerable deviation from the experimental observations, as is shown in Figure 9. Although an increasing N_2 fraction leads to more electron energy being converted into vibrational excitation (Figure 7), which promotes the forward Zeldovich N_2+O reaction rate coefficient, the difference between the thermal and non-thermal model results is lowest at an N_2 fraction of 90%. This is because the limited O_2 concentration restricts the utilisation of

vibrational energy for NO formation. Moreover, the gas temperature within the plasma core increases at higher N_2 fractions, accelerating vibrational energy loss through V–T relaxation processes. Most of the vibrational energy is eventually lost through V-T relaxation.

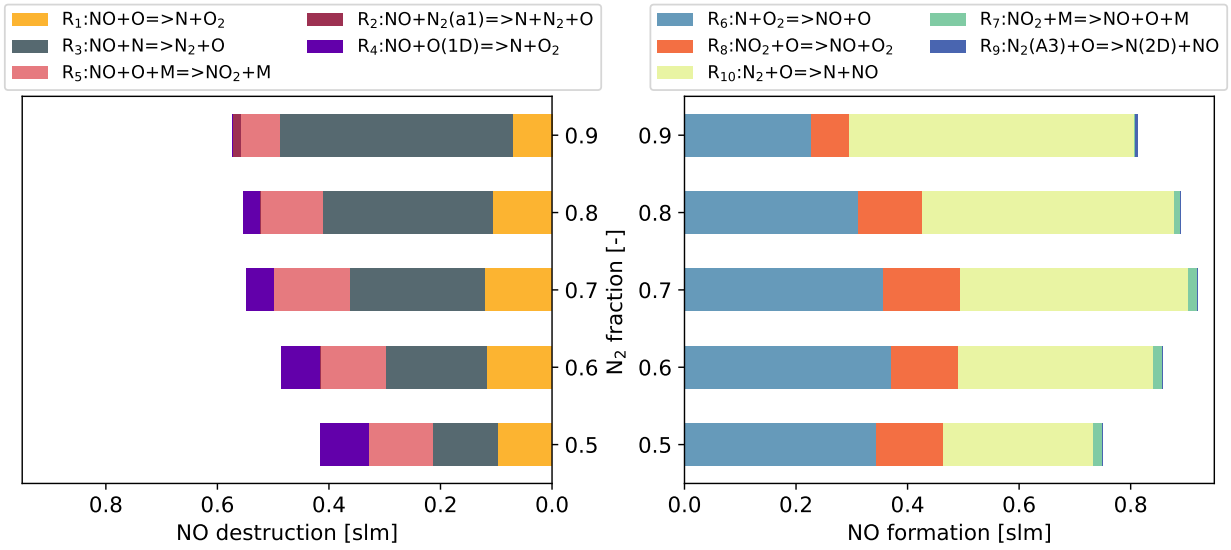

Figure 10: Cumulative reaction product for the four most important reactions related to NO formation and destruction under varying initial gas ratios in the whole process, including discharge and afterglow.

To better understand NO synthesis, it is essential to examine the key reactions responsible for NO formation and destruction. Figure 10 presents the four most significant reactions under varying N_2 fractions, encompassing both the discharge and afterglow domains. At a N_2 fraction of 90%, over 60% of NO is produced via the reaction R_{10} (in Figure 10). Due to the limited O_2 content under this condition, nearly 70% of the resulting N atoms do not proceed through the subsequent Zeldovich reaction chain (*i.e.*, the reaction R_6) . As a result, the contribution of the reaction R_6 is much lower than that of reaction R_{10}. In contrast, most N atoms are consumed through reaction R_3, making this pathway the dominant route for NO destruction. While a fraction of NO reacts with O atoms to form NO_2 via the reaction R_5, nearly all NO_2 subsequently recombines with other O atoms, regenerating NO and O_2 by the reaction R_8. In this cycle, NO effectively acts as a catalyst, promoting the recombination of O atoms into O_2.[67] The fourth most important reactions contributing to NO formation

and destruction have a negligible impact, suggesting that nearly all NO synthesis can be attributed to the key reactions discussed above.

As the O_2 fraction increases, the reaction R_6 plays an increasingly significant role in NO formation. Accordingly, less NO is destroyed by N atoms via the reaction R_3. The additional O_2 also leads to increased O atom production through dissociation, which accelerates both the reaction R_5 and the subsequent reaction R_8. A higher concentration of O atoms also enhances the formation of excited $O(^1D)$, thereby increasing the yield of the reaction R_4. Furthermore, the reaction R_9, which typically plays a more significant role in NO formation at low pressures,[90] becomes less prominent than NO_2 dissociation at higher O_2 fractions. The total cumulative reaction product associated with NO formation reaches the maximum at a N_2 fraction of 70%. Below this threshold, the contribution from the reaction R_{10} decreases significantly and eventually falls below that of the reaction R_6 at a 50% N_2 fraction. In contrast, the overall cumulative amount of NO destruction exhibits a monotonic decrease with decreasing N_2 fraction, indicating that lower nitrogen content suppresses NO decomposition pathways more consistently than it affects formation pathways.

How to reduce the energy cost further?

Although NO_x synthesis and energy transfer have been discussed in detail, further efforts are required to identify strategies for performance improvement. In another warm plasma, experiments have proved that expanding the plasma region of GA discharges by treating more initial gas, including rotating plasmas,[21,24] using a vortex flow,[41,91] and using external magnetic fields[17,92] can improve the reactor performance further. Therefore, it is necessary to explore the effect of the plasma size of the MW discharge on the performance.

In MW plasma systems, the spatial extent of the discharge, particularly its radial width, is strongly influenced by the skin depth.[74] According to MW propagation theory discussed by Den Harder *et al.*,[93] the skin depth is inversely proportional to the MW frequency. Therefore, plasma radius may alter with different MW frequencies. Figure 11 investigates the energy

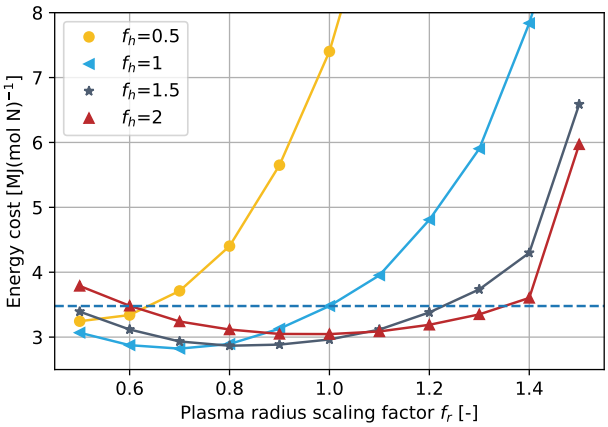

Figure 11: Energy cost as a function of plasma radius scaling factor f_r and plasma length scaling factor f_h for 50% N_2 fraction. The scaling factor is defined as the ratio of the new radius (or height) to the original radius (or height). The blue dashed line represents the baseline under f_h=f_r=1.

costs at various plasma radii under a fixed input power. The plasma radius scaling factor f_r is defined as the ratio of the current radius to the original radius (8.4 mm). Under the original plasma length condition, although a lower plasma radius scaling factor results in a smaller volume of gas being treated, the corresponding increase in power density within the plasma core still enhances total NO production. The minimum energy cost is achieved at 70% of the current plasma radius, reaching 2.8 MJ(mol N)$^{-1}$. However, it is also observed that excessive power density may lead to increased energy costs. This occurs when a larger portion of the input energy is diverted toward gas heating rather than driving NO formation. Elevated gas temperatures not only diminish vibrational excitation effects—primarily due to enhanced V-T relaxation—but also promote NO destruction.

Except for the radius, the plasma length is another parameter to change the size of the plasma region. Kelly *et al.* reported that plasma length increases with rising MW power, which consequently extends the residence time.[46] Figure 11 reveals the relation between plasma length and energy cost. For simplicity, it is assumed that the peak power density in Eq.(2) remains constant for a fixed plasma radius across different plasma lengths. As a result, the total input power increases with plasma length. The plasma height scaling

factor f_h is defined as the ratio of the current height to the original height (40 mm). Under the original plasma radius condition, the minimum energy cost is obtained at 1.5 times the original plasma length. For the longer plasma length (f_h=2), the extended residence time enhances the NO destruction pathways, thereby reducing the overall NO yield. Moreover, as the plasma radius decreases, the negative impact of extended residence time on NO formation becomes more pronounced, likely due to increased thermal decomposition and reduced vibrational excitation efficiency. Overall, the current combination of power density and residence time remains insufficient to fully exploit vibrational or thermal energy for efficient NO synthesis. These findings underscore the importance of optimising the plasma geometry and energy input to achieve an optimal balance between power density, reaction selectivity, and energy cost.

A fast cooling in the afterglow via adding a nozzle or cold quenching gas can prevent NO destruction and decrease the energy cost accordingly[28,31] at atmospheric pressure. However, since the NO destruction in the afterglow is already nearly zero in the current case due to its low gas temperature (Figure 5), the simulation has proved that a higher cooling rate fails to improve the performance at intermediate pressure. Another promising strategy to enhance NO_x production is to exploit plasma–catalyst synergy by placing the catalyst in the afterglow region. The primary role of the catalyst is generally considered to be the provision of active sites for the adsorption of reactive species that participate in NO_x synthesis reactions.[94] A wide variety of reactive neutral species produced in the discharge region, including electronically excited N_2, vibrationally excited N_2, and atomic species, retain sufficient reactivity within the afterglow. These species can participate in subsequent surface reactions on the catalyst, thereby promoting N_x fixation.[95] Last but not least, compared to continuous MW discharge, pulse-modulated MW discharge offers significant advantages for plasma-assisted nitrogen fixation.[44,96] Pulse modulation could effectively decrease gas temperature, suppressing V-T relaxation.[48] This important property makes more vibrational energy used for overcoming the Zeldovich reaction barriers and thereby enhancing NO production.

Conclusion

This study offers a detailed understanding of NO synthesis in microwave plasma sustained in N_2–O_2 mixtures at intermediate pressure, achieved through the integration of experimental diagnostics with quasi-1.5D physico-chemical modeling. A series of experimental results, including energy cost, NO_x yield, and corresponding plasma size, are first presented for varying N_2 content at 80 mbar. Strong non-thermal behaviour, driven by electron impact collisions, is observed in the plasma core and enhances NO production. The optimal conditions for energy cost are obtained in a $\sim$60% N_2 mixture. Although greater electron energy is transferred into N_2 vibrational modes with increasing N_2 content, the limited availability of O_2 and the elevated gas temperature in the plasma core constrain the beneficial effects of non-thermal excitation on NO formation.

Additionally, diffusion plays a critical role in maintaining NO yields. The results show that NO is primarily formed in the plasma region, and diffusion transports NO molecules outward, thereby suppressing NO destruction and reinforcing the forward Zeldovich mechanism in the core. Reaction pathway analysis reveals that at high N_2 fractions, NO formation is primarily driven by the forward Zeldovich N_2+O reaction, while NO losses are dominated by the reverse Zeldovich NO+N reaction. The total reaction products associated with NO formation reach a maximum at a 70% N_2 fraction, whereas those related to NO destruction decrease monotonically with decreasing N_2 content. As a result, the net NO production is maximized at a 60% N_2 fraction.

Various strategies to reduce the energy cost of microwave plasma-assisted NO synthesis are discussed. The spatial dimensions of the plasma, particularly its radial width and axial length, play a crucial role in the energy distribution and NO yield. Reducing the plasma radius to about 70% of its original value increases the power density within the core, thereby improving energy cost even though a smaller gas volume is processed. Extending the plasma column increases the residence time, which initially enhances NO formation but can ultimately promote its thermal decomposition when the residence time becomes too long.

Hence, optimization requires a fine balance between power density, reaction selectivity, and residence time to minimize overall energy consumption. By integrating the present model with machine learning techniques, it becomes possible to predict the optimal plasma dimensions and corresponding operating parameters that achieve optimal energy cost and NO_x yield. Although rapid cooling in the afterglow can effectively suppress NO destruction under high-pressure conditions, its impact is limited in the present case due to the already low level of NO destruction at intermediate pressure.

Overall, the present study provides a mechanistic understanding and predictive modeling that are relevant to the future design of industrial nitrogen fixation systems. Specifically, our results show that plasma geometry strongly affects power density, residence time, and energy cost. This highlights the importance of plasma-shape optimization in large-scale reactors, where controlling the distribution of power density and diffusion is critical for maximizing NO_x yield while minimizing energy cost. Moreover, the identification of optimal feed composition provides practical guidance for gas mixing strategies that can be translated to air-based operation. The role of diffusion in transporting NO away from the plasma core and suppressing its destruction further suggests that reactor designs promoting efficient mixing and radial transport could impact overall energy cost at scale. We believe that these insights can thus guide the development of optimized plasma sources with tailored geometries and gas flow strategies for energy-efficient nitrogen fixation.

Acknowledgement

This work was financially supported by the China Scholarship Council (No. CSC202106240037). VG was partially supported by FCT – Fundação para a Ciência e Tecnologia under the projects UIDB/50010/2020
(https://doi.org/10.54499/UIDB/50010/2020),
UIDP/50010/2020 (https://doi.org/10.54499/UIDP/50010/2020),

LA/P/0061/2020 (https://doi.org/10.54499/LA/P/0061/2020), and
PTDC/FIS-PLA/1616/2021 (https://doi.org/10.54499/PTDC/FIS-PLA/1616/2021).

References

(1) Snoeckx, R.; Bogaerts, A. Plasma technology–a novel solution for CO_2 conversion? *Chemical Society Reviews* **2017**, *46*, 5805–5863.

(2) Anastasopoulou, A.; Keijzer, R.; Butala, S.; Lang, J.; van Rooij, G.; Hessel, V. Eco-efficiency analysis of plasma-assisted nitrogen fixation. *Journal of Physics D: Applied Physics* **2020**, *53*, 234001.

(3) Smith, C.; Hill, A. K.; Torrente-Murciano, L. Current and future role of Haber–Bosch ammonia in a carbon-free energy landscape. *Energy & Environmental Science* **2020**, *13*, 331–344.

(4) Fernandez, C. A.; Chapman, O.; Brown, M. A.; Alvarez-Pugliese, C. E.; Hatzell, M. C. Achieving decentralized, electrified, and decarbonized ammonia production. *Environmental Science & Technology* **2024**, *58*, 6964–6977.

(5) Smith, C.; Torrente-Murciano, L. The importance of dynamic operation and renewable energy source on the economic feasibility of green ammonia. *Joule* **2024**, *8*, 157–174.

(6) Pfromm, P. H. Towards sustainable agriculture: Fossil-free ammonia. *Journal of Renewable and Sustainable Energy* **2017**, *9*, 1–20.

(7) Lim, J.; Fernández, C. A.; Lee, S. W.; Hatzell, M. C. Ammonia and nitric acid demands for fertilizer use in 2050. *ACS Energy Letters* **2021**, *6*, 3676–3685.

(8) Cherkasov, N.; Ibhadon, A.; Fitzpatrick, P. A review of the existing and alternative methods for greener nitrogen fixation. *Chemical Engineering and Processing: Process Intensification* **2015**, *90*, 24–33.

(9) Rouwenhorst, K. H.; Jardali, F.; Bogaerts, A.; Lefferts, L. From the Birkeland–Eyde process towards energy-efficient plasma-based NO_x synthesis: a techno-economic analysis. *Energy & environmental science* **2021**, *14*, 2520–2534.

(10) Abdelaziz, A. A.; Komuro, A.; Teramoto, Y.; Schiorlin, M.; Kim, D.-Y.; Nozaki, T.; Kim, H.-H. Atmospheric-Pressure Plasmas for NO_x Production; Short Review on Current Status. *Current Opinion in Green and Sustainable Chemistry* **2024**, 100977.

(11) Yang, Y.; Murphy, A. B. CO_2 conversion using non-thermal plasmas: the path towards industrialisation. *Current Opinion in Green and Sustainable Chemistry* **2024**, 100994.

(12) Kelly, S.; Verheyen, C.; Cowley, A.; Bogaerts, A. Producing oxygen and fertilizer with the Martian atmosphere by using microwave plasma. *Chem* **2022**, *8*, 2797–2816.

(13) Bogaerts, A.; Neyts, E. C. Plasma technology: an emerging technology for energy storage. *ACS Energy Letters* **2018**, *3*, 1013–1027.

(14) Winter, L. R.; Chen, J. G. N_2 fixation by plasma-activated processes. *Joule* **2021**, *5*, 300–315.

(15) Chen, J. G.; Crooks, R. M.; Seefeldt, L. C.; Bren, K. L.; Bullock, R. M.; Darensbourg, M. Y.; Holland, P. L.; Hoffman, B.; Janik, M. J.; Jones, A. K.; others Beyond fossil fuel–driven nitrogen transformations. *Science* **2018**, *360*, eaar6611.

(16) Bogaerts, A. Plasma technology for the electrification of chemical reactions. *Nature Chemical Engineering* **2025**, 1–5.

(17) Zhang, Y.; Liu, B.; Luo, J.; Nie, L.; Xian, Y.; Lu, X. Research on key influencing factors and mechanisms of improved nitrogen fixation efficiency in magnetic-driven gliding arc. *Journal of Physics D: Applied Physics* **2023**, *57*, 125204.

(18) Esposito, F. On the relevance of accurate input data for vibrational kinetics in air cold

plasmas: the case of nitrogen fixation. *Plasma Sources Science and Technology* **2022**, *31*, 094010.

(19) MacFarlane, D. R.; Cherepanov, P. V.; Choi, J.; Suryanto, B. H.; Hodgetts, R. Y.; Bakker, J. M.; Vallana, F. M. F.; Simonov, A. N. A roadmap to the ammonia economy. *Joule* **2020**, *4*, 1186–1205.

(20) Rouwenhorst, K. H.; Jardali, F.; Bogaerts, A.; Lefferts, L. Correction: From the Birkeland–Eyde process towards energy-efficient plasma-based NO_x synthesis: a techno-economic analysis. *Energy & environmental science* **2023**, *16*, 6170–6173.

(21) Jardali, F.; van Alphen, S.; Creel, J.; Eshtehardi, H. A.; Axelsson, M.; Ingels, R.; Snyders, R.; Bogaerts, A. NO_x production in a rotating gliding arc plasma: Potential avenue for sustainable nitrogen fixation. *Green Chemistry* **2021**, *23*, 1748–1757.

(22) Pei, X.; Gidon, D.; Yang, Y.-J.; Xiong, Z.; Graves, D. B. Reducing energy cost of NO_x production in air plasmas. *Chemical Engineering Journal* **2019**, *362*, 217–228.

(23) Lei, X.; Cheng, H.; Nie, L.; Lu, X. Nitrogen fixation as NO_x enabled by a three-level coupled rotating electrodes air plasma at atmospheric pressure. *Plasma Chemistry and Plasma Processing* **2022**, *42*, 211–227.

(24) Chen, H.; Wu, A.; Mathieu, S.; Gao, P.; Li, X.; Xu, B. Z.; Yan, J.; Tu, X. Highly efficient nitrogen fixation enabled by an atmospheric pressure rotating gliding arc. *Plasma Processes and Polymers* **2021**, *18*, 2000200.

(25) Patil, B. S.; Peeters, F. J. J.; van Rooij, G. J.; Medrano, J.; Gallucci, F.; Lang, J.; Wang, Q.; Hessel, V. Plasma assisted nitrogen oxide production from air: Using pulsed powered gliding arc reactor for a containerized plant. *AIChE Journal* **2018**, *64*, 526–537.

(26) Angineni, J.; Reddy, P. M. K.; Anga, S.; Somaiah, P. V. Sustainable nitrogen fixation by novel gliding arc plasma reactor for the production of nitrogen fertilizers. *Plasma Processes and Polymers* **2024**, *21*, 2400059.

(27) Angineni, J.; Reddy, P. M. K.; Anga, S.; Somaiah, P. V. Nitrogen Fixation by Simple Gling Arc Plasma Reactor at Elevated Pressure for Synthesis of Aqueous Nitrogen Fertilizer. *Plasma Processes and Polymers* **2025**, *22*, 2400209.

(28) van Alphen, S.; Eshtehardi, H. A.; O'Modhrain, C.; Bogaerts, J.; van Poyer, H.; Creel, J.; Delplancke, M.-P.; Snyders, R.; Bogaerts, A. Effusion nozzle for energy-efficient NO_x production in a rotating gliding arc plasma reactor. *Chemical engineering journal* **2022**, *443*, 136529.

(29) Wang, W.; Patil, B.; Heijkers, S.; Hessel, V.; Bogaerts, A. Nitrogen fixation by gliding arc plasma: better insight by chemical kinetics modelling. *ChemSusChem* **2017**, *10*, 2145–2157.

(30) Li, Z.; Nie, L.; Liu, D.; Lu, X. An atmospheric pressure glow discharge in air stabilized by a magnetic field and its application on nitrogen fixation. *Plasma Processes and Polymers* **2022**, *19*, 2200071.

(31) Majeed, M.; Iqbal, M.; Altin, M.; Kim, Y.-N.; Dinh, D. K.; Lee, C.; Ali, Z.; Lee, D. H. Effect of thermal gas quenching on NO_x production by atmospheric pressure rotating arc Plasma: A pathway towards Eco-Friendly fertilizer. *Chemical Engineering Journal* **2024**, *485*, 149727.

(32) van Alphen, S.; Jardali, F.; Creel, J.; Trenchev, G.; Snyders, R.; Bogaerts, A. Sustainable gas conversion by gliding arc plasmas: a new modelling approach for reactor design improvement. *Sustainable Energy & Fuels* **2021**, *5*, 1786–1800.

(33) Namihira, T.; Katsuki, S.; Hackam, R.; Akiyama, H.; Okamoto, K. Production of nitric

oxide using a pulsed arc discharge. *IEEE Transactions on plasma science* **2003**, *30*, 1993–1998.

(34) Denra, A.; Saud, S.; Nguyen, D. B.; Trinh, Q. T.; Nguyen, T.-K.; An, H.; Nguyen, N.-T.; Teke, S.; Mok, Y. S. Nitrogen fixation by rotational gliding arc plasma at surrounding conditions. *Journal of Cleaner Production* **2024**, *436*, 140618.

(35) Patil, B.; Rovira Palau, J.; Hessel, V.; Lang, J.; Wang, Q. Plasma nitrogen oxides synthesis in a milli-scale gliding arc reactor: investigating the electrical and process parameters. *Plasma Chemistry and Plasma Processing* **2016**, *36*, 241–257.

(36) Tsonev, I.; O'Modhrain, C.; Bogaerts, A.; Gorbanev, Y. Nitrogen fixation by an arc plasma at elevated pressure to increase the energy efficiency and production rate of NO_x. *ACS Sustainable Chemistry & Engineering* **2023**, *11*, 1888–1897.

(37) van Raak, T.; van den Bogaard, H.; De Felice, G.; Emmery, D.; Gallucci, F.; Li, S. Numbering up and sizing up gliding arc reactors to enhance the plasma-based synthesis of NO_x. *Catalysis Science & Technology* **2024**, *14*, 5405–5421.

(38) Li, S.; van Raak, T.; Kriek, R.; De Felice, G.; Gallucci, F. Gliding Arc Reactor under AC Pulsed Mode Operation: Spatial Performance Profile for NO_x Synthesis. *ACS Sustainable Chemistry & Engineering* **2023**, *11*, 12821–12832.

(39) van Raak, T.; Gallucci, F.; Li, S. The impact of current-limiting resistors on NO_x synthesis in a plasma-based process with a gliding arc reactor. *Journal of Physics D: Applied Physics* **2025**, *58*, 245203.

(40) Sun, Z.; Zheng, H.; Zheng, X.; Tang, J.; Zhao, Z.; Li, J. Improvement on the Energy Efficiency of NO_x Synthesis in Pulsed Discharge Plasma: A Focus on the Modulation by Pulse Rise Rate and Pulse Repetition Frequency. *ACS Sustainable Chemistry & Engineering* **2025**,

(41) Vervloessem, E.; Aghaei, M.; Jardali, F.; Hafezkhiabani, N.; Bogaerts, A. Plasma-based N_2 fixation into NO_x: insights from modeling toward optimum yields and energy costs in a gliding arc plasmatron. *ACS Sustainable Chemistry & Engineering* **2020**, *8*, 9711–9720.

(42) Azizov, R.; Zhivotov, V.; Krotov, M.; Rusanov, V.; Tarasov, Y.; Fridma, A. Synthesis of nitrogen oxides in a nonequilibrium microwave discharge under electron-cyclotron resonance conditions. *Khimiya Vysok. Energii* **1980**, *14*, 366–8.

(43) Mutel, B.; Dessaux, O.; Goudmand, P. Energy cost improvement of the nitrogen oxides synthesis in a low pressure plasma. *Revue de physique appliquée* **1984**, *19*, 461–464.

(44) Samadi Bahnamiri, O.; Verheyen, C.; Snyders, R.; Bogaerts, A.; Britun, N. Nitrogen fixation in pulsed microwave discharge studied by infrared absorption combined with modelling. *Plasma Sources Science and Technology* **2021**, *30*, 065007.

(45) Sun, J.; Zhang, T.; Hong, J.; Zhou, R.; Masood, H.; Zhou, R.; Murphy, A. B.; Ostrikov, K. K.; Cullen, P. J.; Lovell, E. C.; others Insights into plasma-catalytic nitrogen fixation from catalyst microanalysis and chemical kinetics modelling. *Chemical Engineering Journal* **2023**, *469*, 143841.

(46) Kelly, S.; Bogaerts, A. Nitrogen fixation in an electrode-free microwave plasma. *Joule* **2021**, *5*, 3006–3030.

(47) Kim, T.; Song, S.; Kim, J.; Iwasaki, R. Formation of NO_x from air and N_2/O_2 mixtures using a nonthermal microwave plasma system. *Japanese journal of applied physics* **2010**, *49*, 126201.

(48) Luo, Y.; Qiu, F.; Zheng, X.; Li, H.; Li, Y.; Shuai, J.; Wang, J.; Zhang, T.; Pei, X. Pulse-modulated microwave air plasma for nitrogen fixation as NO_x. *Journal of Physics D: Applied Physics* **2024**,

(49) Zheng, F.; Feng, K.; Wu, S.; Xiao, W. Experimental Investigation into Atmospheric Microwave Plasma-Driven Nitrogen Fixation Using Metal–Organic Frameworks. *Processes* **2024**, *12*, 2633.

(50) Wu, S.; Liao, Y.; Feng, K.; Zheng, F.; Xiao, W. Nitrogen fixation by atmospheric microwave plasma with local electric field enhancement. *Journal of Physics D: Applied Physics* **2024**, *58*, 015205.

(51) Feng, K.; Wu, S.; Zheng, F.; Xiao, W. A novel atmospheric microwave plasma source based on circular waveguide with double ridges for nitrogen fixation. *Physica Scripta* **2024**, *100*, 015611.

(52) Janda, M.; Martišovitš, V.; Hensel, K.; Machala, Z. Generation of antimicrobial NO_x by atmospheric air transient spark discharge. *Plasma Chemistry and Plasma Processing* **2016**, *36*, 767–781.

(53) Abdelaziz, A. A.; Teramoto, Y.; Nozaki, T.; Kim, H.-H. Performance of high-frequency spark discharge for efficient NO_x production with tunable selectivity. *Chemical Engineering Journal* **2023**, *470*, 144182.

(54) Zhang, S.; Zong, L.; Zeng, X.; Zhou, R.; Liu, Y.; Zhang, C.; Pan, J.; Cullen, P. J.; Ostrikov, K. K.; Shao, T. Sustainable nitrogen fixation with nanosecond pulsed spark discharges: insights into free-radical-chain reactions. *Green Chemistry* **2022**, *24*, 1534–1544.

(55) Li, J.; Yao, S.; Wu, Z. NO_x production in plasma reactors by pulsed spark discharges. *Journal of Physics D: Applied Physics* **2020**, *53*, 385201.

(56) Pavlovich, M.; Ono, T.; Galleher, C.; Curtis, B.; Clark, D.; Machala, Z.; Graves, D. Air spark-like plasma source for antimicrobial NO_x generation. *Journal of Physics D: Applied Physics* **2014**, *47*, 505202.

(57) Abdelaziz, A. A.; Teramoto, Y.; Nozaki, T.; Kim, H.-H. Toward reducing the energy cost of NO_x formation in a spark discharge reactor through pinpointing its mechanism. *ACS Sustainable Chemistry & Engineering* **2023**, *11*, 4106–4118.

(58) Malik, M. A.; Jiang, C.; Heller, R.; Lane, J.; Hughes, D.; Schoenbach, K. H. Ozone-free nitric oxide production using an atmospheric pressure surface discharge–a way to minimize nitrogen dioxide co-production. *Chemical Engineering Journal* **2016**, *283*, 631–638.

(59) Ma, Y.; Wang, Y.; Harding, J.; Tu, X. Plasma-enhanced N_2 fixation in a dielectric barrier discharge reactor: effect of packing materials. *Plasma Sources Science and Technology* **2021**, *30*, 105002.

(60) Li, Y.; Qin, L.; Wang, H.-L.; Li, S.-S.; Yuan, H.; Yang, D.-Z. High efficiency NO_x synthesis and regulation using dielectric barrier discharge in the needle array packed bed reactor. *Chemical Engineering Journal* **2023**, *461*, 141922.

(61) Bogaerts, A.; Snoeckx, R.; Trenchev, G.; Wang, W. In *Plasma Chemistry and Gas Conversion*; Britun, N., Silva, T., Eds.; IntechOpen: London, 2018; Chapter 2.

(62) Andersen, J.; van't Veer, K.; Christensen, J.; Østberg, M.; Bogaerts, A.; Jensen, A. Ammonia decomposition in a dielectric barrier discharge plasma: Insights from experiments and kinetic modeling. *Chemical Engineering Science* **2023**, *271*, 118550.

(63) Armenise, I. Low temperature state-to-state vibrational kinetics of O+ N_2(v) and N+ O_2(v) collisions. *Chemical Physics* **2023**, *571*, 111937.

(64) Armenise, I.; Esposito, F. N+ O_2(v) collisions: reactive, inelastic and dissociation rates for state-to-state vibrational kinetic models. *Chemical Physics* **2021**, *551*, 111325.

(65) Esposito, F.; Armenise, I. Reactive, inelastic, and dissociation processes in collisions of

atomic oxygen with molecular nitrogen. *The Journal of Physical Chemistry A* **2017**, *121*, 6211–6219.

(66) Altin, M.; Viegas, P.; Vialetto, L.; van Rooij, G.; Diomede, P. Spatio-temporal analysis of power deposition and vibrational excitation in pulsed N_2 microwave discharges from 1D fluid modelling and experiments. *Plasma Sources Science and Technology* **2024**, *33*, 045008.

(67) Shen, Q.; Pikalev, A.; Peeters, F.; Guerra, V.; van de Sanden, M. C. M. Pinpointing energy transfer mechanisms in the quenching process of microwave air plasma. *Journal of Physics D: Applied Physics* **2025**, *58*, 275203.

(68) van Poyer, H. M.; Tsonev, I.; Maerivoet, S. J.; Albrechts, M. C.; Bogaerts, A. Influence of radial transport and turbulent effects on CO_2 conversion in a microwave plasma reactor: Insights from a multi-dimensional thermo-chemical flow model. *Chemical Engineering Journal* **2025**, *507*, 160688.

(69) Mercer, E. R.; van Alphen, S.; van Deursen, C.; Righart, T.; Bongers, W.; Snyders, R.; Bogaerts, A.; van de Sanden, M. C. M.; Peeters, F. J. J. Post-plasma quenching to improve conversion and energy efficiency in a CO_2 microwave plasma. *Fuel* **2023**, *334*, 126734.

(70) Shen, Q.; Pikalev, A.; Gans, J.; Kuijpers, L.; Guerra, V.; van de Sanden, M. C. M. Boosting the NO_x production in microwave air plasma: A synergy of chemistry and vibrational kinetics. *Plasma Sources Science and Technology* **2026**, doi: 10.1088/1361–6595/ae2d91.

(71) Tatar, M.; Vashisth, V.; Iqbal, M.; Butterworth, T.; van Rooij, G.; Andersson, R. Analysis of a plasma reactor performance for direct nitrogen fixation by use of three-dimensional simulations and experiments. *Chemical Engineering Journal* **2024**, *497*, 154756.

(72) Wolf, A. J.; Righart, T. W.; Peeters, F. J. J.; Bongers, W.; van de Sanden, M. C. M. Implications of thermo-chemical instability on the contracted modes in CO_2 microwave plasmas. *Plasma Sources Science and Technology* **2020**, *29*, 025005.

(73) Rothman, L. S.; Gordon, I. E.; Barbe, A.; Benner, D. C.; Bernath, P. F.; Birk, M.; Boudon, V.; Brown, L. R.; Campargue, A.; Champion, J.-P.; others The HITRAN 2008 molecular spectroscopic database. *Journal of Quantitative Spectroscopy and Radiative Transfer* **2009**, *110*, 533–572.

(74) Wolf, A. J.; Peeters, F. J. J.; Groen, P.; Bongers, W.; van de Sanden, M. C. M. CO_2 conversion in nonuniform discharges: Disentangling dissociation and recombination mechanisms. *The Journal of Physical Chemistry C* **2020**, *124*, 16806–16819.

(75) Guerra, V.; Tejero-del Caz, A.; Pintassilgo, C. D.; Alves, L. L. Modelling N_2–O_2 plasmas: volume and surface kinetics. *Plasma Sources Science and Technology* **2019**, *28*, 073001.

(76) Viegas, P.; Vialetto, L.; Wolf, A.; Peeters, F. J. J.; Groen, P.; Righart, T.; Bongers, W.; van de Sanden, M. C. M.; Diomede, P. Insight into contraction dynamics of microwave plasmas for CO_2 conversion from plasma chemistry modelling. *Plasma Sources Science and Technology* **2020**, *29*, 105014.

(77) Wang, X.; Hong, Q.; Hu, Y.; Sun, Q. On the accuracy of two-temperature models for hypersonic nonequilibrium flow. *Acta Mechanica Sinica* **2023**, *39*, 122193.

(78) Kee, R. J.; Coltrin, M. E.; Glarborg, P. *Chemically reacting flow: theory and practice*; John Wiley & Sons, 2005.

(79) Shen, Q.; Pikalev, A.; Peeters, F.; Gans, J.; van de Sanden, M. C. M. Two-temperature model of the non-thermal chemical dissociation of CO_2. *Reaction Chemistry & Engineering* **2025**, *10*, 146–157.

(80) Tejero-del Caz, A.; Guerra, V.; Gonçalves, D.; Da Silva, M. L.; Marques, L.; Pinhao, N.; Pintassilgo, C. D.; Alves, L. L. The lisbon kinetics boltzmann solver. *Plasma Sources Science and Technology* **2019**, *28*, 043001.

(81) Tejero-del Caz, A.; Guerra, V.; Pinhão, N.; Pintassilgo, C. D.; Alves, L. L. On the quasi-stationary approach to solve the electron Boltzmann equation in pulsed plasmas. *Plasma Sources Science and Technology* **2021**, *30*, 065008.

(82) Goodwin, D. G.; Moffat, H. K.; Schoegl, I.; Speth, R. L.; Weber, B. W. Cantera: An Object-oriented Software Toolkit for Chemical Kinetics, Thermodynamics, and Transport Processes. `https://www.cantera.org`, 2023; Version 3.0.0.

(83) Adamovich, I. V.; Macheret, S. O.; Rich, J. W.; Treanor, C. E. Vibrational energy transfer rates using a forced harmonic oscillator model. *Journal of Thermophysics and Heat Transfer* **1998**, *12*, 57–65.

(84) Esposito, F.; Armenise, I.; Capitelli, M. N–N_2 state to state vibrational-relaxation and dissociation rates based on quasiclassical calculations. *Chemical Physics* **2006**, *331*, 1–8.

(85) See `http://esther.ist.utl.pt/pages/stellar.php` for STELLAR database.

(86) Hong, Q.; Bartolomei, M.; Pirani, F.; Esposito, F.; Sun, Q.; Coletti, C. Vibrational deactivation in O(3P)+ N_2 collisions: from an old problem towards its solution. *Plasma Sources Science and Technology* **2022**, *31*, 084008.

(87) Kotov, V.; Kiefer, C. K.; Hecimovic, A. Validation of the thermo-chemical approach to modelling of the CO_2 conversion in sub-atmospheric pressure microwave gas discharges. *Plasma Sources Science and Technology* **2023**,

(88) Synek, P.; Obrusník, A.; Hübner, S.; Nijdam, S.; Zajíčková, L. On the interplay of gas

dynamics and the electromagnetic field in an atmospheric Ar/H_2 microwave plasma torch. *Plasma Sources Science and Technology* **2015**, *24*, 025030.

(89) Ansys fluent theory guide. *Ansys Inc., USA* **2011**, *15317*, 724–746.

(90) Guerra, V.; Sa, P.; Loureiro, J. Role played by the $N_2(A3\Sigma u^+)$ metastable in stationary N_2 and N_2-O_2 discharges. *Journal of Physics D: Applied Physics* **2001**, *34*, 1745.

(91) Trenchev, G.; Kolev, S.; Bogaerts, A. A 3D model of a reverse vortex flow gliding arc reactor. *Plasma Sources Science and Technology* **2016**, *25*, 035014.

(92) Wang, C.; Lu, Z.; Li, D.; Xia, W.; Xia, W. Effect of the magnetic field on the magnetically stabilized gliding arc discharge and its application in the preparation of carbon black nanoparticles. *Plasma Chemistry and Plasma Processing* **2018**, *38*, 1223–1238.

(93) den Harder, N.; van den Bekerom, D. C.; Al, R. S.; Graswinckel, M. F.; Palomares, J. M.; Peeters, F. J.; Ponduri, S.; Minea, T.; Bongers, W. A.; van de Sanden, M. C. M.; others Homogeneous CO_2 conversion by microwave plasma: wave propagation and diagnostics. *Plasma Processes and Polymers* **2017**, *14*, 1600120.

(94) Peng, P.; Schiappacasse, C.; Zhou, N.; Addy, M.; Cheng, Y.; Zhang, Y.; Ding, K.; Wang, Y.; Chen, P.; Ruan, R. Sustainable non-thermal plasma-assisted nitrogen fixation—synergistic catalysis. *ChemSusChem* **2019**, *12*, 3702–3712.

(95) Pei, X.; Li, Y.; Luo, Y.; Man, C.; Zhang, Y.; Lu, X.; Graves, D. B. Nitrogen fixation as NO_x using air plasma coupled with heterogeneous catalysis at atmospheric pressure. *Plasma Processes and Polymers* **2024**, *21*, 2300135.

(96) van Alphen, S.; Vermeiren, V.; Butterworth, T.; van den Bekerom, D. C.; van Rooij, G.; Bogaerts, A. Power pulsing to maximize vibrational excitation efficiency in N_2 microwave plasma: a combined experimental and computational study. *The Journal of Physical Chemistry C* **2019**, *124*, 1765–1779.

Mechanistic Insights into NO_x Production in Microwave Plasma at Intermediate Pressure

Qinghao Shen,[†,‡] Lex Kuijpers,[†,‡] Jonas Gans,[†,‡] Serguei Starostine,[†] Vasco Guerra,[¶] and Mauritius C.M. van de Sanden[*,†,‡]

†*Dutch Institute for Fundamental Energy Research, Eindhoven, The Netherlands*

‡*Department of Applied Physics, Eindhoven Institute of Renewable Energy Systems, Eindhoven University of Technology, Eindhoven, The Netherlands*

¶*Instituto de Plasmas e Fusão Nuclear, Instituto Superior Técnico, Universidade de Lisboa, Lisboa, Portugal*

E-mail: m.c.m.v.d.sanden@tue.nl

Supplementary Data for Publication

Number of pages: 9

Number of figures: 4

How to optimise computational cost?

Although the MT method is widely used in CFD modelling due to its lower computational cost compared to the State-to-State approach,[1] further reduction in computational cost is still required to enable the extension of current simulations to higher-dimensional models coupled with Navier-Stokes solvers in future studies. Previous work has shown that the vibrational temperature of O_2 remains close to the gas temperature in the whole process domain, even at the plasma core.[2] Thus, it is reasonable to assume thermal equilibrium for O_2 vibrations, *i.e.*, the vibrational temperature of O_2 is equal to the gas temperature, while the vibrational excitation of N_2 is treated separately. In this approach, the electron energy originally transferred for O_2 vibrational excitation is redirected to gas heating. The results show that the difference in NO_x production remains below 0.5% between models with and without considering vibrational excitation of O_2, while the computational cost is reduced by more than 50%. Actually, this assumption is particularly appropriate at higher pressures. Firstly, enhanced V-T relaxation at elevated pressures further minimises the temperature gap between gas and vibrational modes,[3] reducing discrepancies between the two models. Secondly, higher pressure leads to a more contracted plasma, resulting in increased power density[4] and significantly elevated gas temperatures in the plasma core.[5,6] For example, under 650 mbar, Tatar *et al.* have reported gas temperatures exceeding 6000 K in the core of an air plasma,[7] where O_2 is almost entirely dissociated within a very short residence time. Therefore, the contribution of O_2 vibrational energy becomes negligible. However, due to the limited amount of remaining O_2, its vibrational temperature becomes highly sensitive to the axial discretization length, which governs the vibrational energy exchange. As model convergence is determined by temperature differences between adjacent steps, this sensitivity can trigger numerous unnecessary recalculations, leading to inefficient computation. Therefore, the reduced non-thermal model offers similar predictive accuracy with significantly improved numerical convergence compared to the full model at higher pressures.

Although a number of the V–V and V–T relaxation processes are omitted by assuming O_2

to be thermalised, the vibrational kinetics still impose substantial computational demands. The energy transfer rate coefficients for the V–V and V–T relaxation processes have been detailed in our previous work.[8] In V–T energy transfer processes, the total V-T power rate coefficient for a specific vibrational level r (*i.e.*, $\sum_w k_{r\to w}\Delta E_{r\to w}$ in Eqs. 24 of the paper[8]) depends solely on V-T rate coefficients $k_{r\to w}$ [in m^3 s^{-1}], and their vibrational energy gaps $\Delta E_{r\to w}$ [in eV]. Importantly, This quantity is independent of the overall vibrational population distribution, and thus can be precomputed for each level. To reduce computational cost, these total energy transfer rates for individual vibrational levels can be tabulated and interpolated during runtime, significantly accelerating the evaluation. This approach reduces the computational complexity from quadratic to linear with respect to the number of vibrational levels.

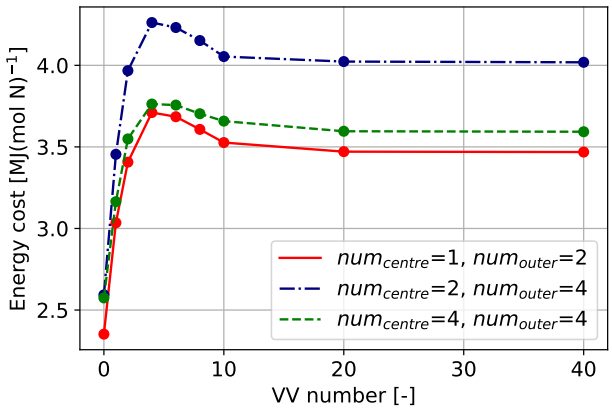

Figure S1: Energy cost versus the number of V–V N_2-O_2 relaxation reactions and PFRs configurations, based on vibrational levels from 0 to m for both N_2 and O_2 (*i.e.*, i and j in the V-V relaxation of Table 2 of the manuscript), at 50% N_2 fraction.

For the V-V energy transfer processes, since the total power rate coefficient for each vibrational level is also related to vibrational population, it cannot interpolate level-specific energy transfer coefficients like V-T relaxation. Actually, V–V N_2–O_2 collisions contribute significantly to the consumption of N_2 vibrational energy, particularly in the discharge region.[2] According to the study by Vervloessem *et al.*,[9] the effect of V–V N_2–O_2 relaxation on NO_x production is highest when the initial gas mixture contains 50% N_2. Simulations

with different numbers of PFRs and varying numbers of V–V relaxation reactions were conducted at 50% initial N_2 fraction, as shown in Figure S1. The results indicate that the number of PFRs in the discharge and outer regions, respectively, affects the total energy cost, which will be further discussed in the next subsection. As the number of vibrational levels decreases from 40 to 20 under different PFRs configurations, the energy cost remains nearly unchanged, suggesting computational redundancy. However, the energy cost initially increases relative to the baseline (*i.e.*, the result with the inclusion of V–V reactions related to first 40 vibrational levels of N_2 and O_2 inclusion) when the number of vibrational level is between 3 and 10, and then drops below the baseline when fewer than 3 vibrational levels are included. When all V–V N_2–O_2 reactions are omitted, the energy cost across different PFRs configurations is approximately 70% of the baseline, consistent with the 0D model findings reported by Vervloessem *et al.*[9] However, as Vervloessem *et al.* mentioned, it is not straightforward to prevent the loss of N_2 vibrational energy via V–V N_2–O_2 relaxation.[9] To maintain a balance between computational efficiency and model accuracy (with an error below 2%), only V–V relaxation processes between N_2 and O_2 involving the first 10 vibrational levels of both species are considered.

What are the optimal numbers of PFRs in the central and outer regions?

Although many methods have been employed to reduce the computational cost of the model, the computational cost is still quite high for the conditions of 32 and 16 PFRs in the central and outer regions, respectively. Since the calculation of the peak turbulence viscosity requires a parameter scan to match the experimental temperature profile, a simplified model that retains sufficient accuracy can accelerate the matching process accordingly. Moreover, because a large-scale parameter scan is also necessary to identify optimal experimental conditions, the simplified model will also enable a substantial reduction in computational cost

for future studies. Therefore, it is crucial to explore the trade-off in computational cost and accuracy.

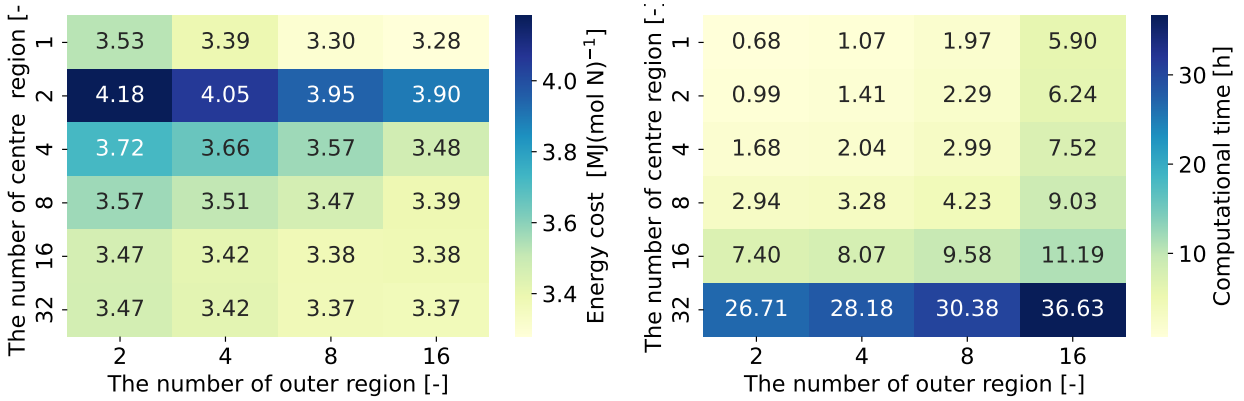

Figure S2: Energy cost and computational time at 50% N_2 fraction, under different PFR number configurations in the central and outer regions, excluding the time required for electron kinetics.

Comparisons of the energy cost and computational time with different numbers of PFR in the central and outer regions are shown in Figure S2. It should be noted that the calculated computational time excludes the time consumed for calculating the electron kinetics. Actually, to balance accuracy and computational efficiency, the new gas composition will be updated to LoKI-B only when the molar fraction of any species (including vibrationally excited states of N_2 and O_2) changes by more than 1% (absolute value) relative to the previously assumed composition. This approach ensures a self-consistent coupling between electron and chemical kinetics, allowing for accurate treatment of gas-phase composition.[10] Furthermore, the new results calculated by the updated gas composition, such as rate coefficients of electron-impact processes, swarm parameters, and electron mean energy, are tabulated and saved. Therefore, if the same gas composition is encountered in the next simulation, the model can directly call the saved data, avoiding the computational cost for LoKI-B. Theoretically, more PFRs in the central region (where electron kinetics should be taken into account) will spend more computational cost on electron kinetics, as it leads to more possibilities of gas composition.

It is noteworthy that, in Figure S2, using a single PFR to simulate the central region can

already yield accurate energy cost predictions, especially when more PFRs are employed in the outer region. However, it is still not recommended due to several inherent limitations. Firstly, the central region typically exhibits pronounced gradients in gas temperature and species concentrations, which cannot be adequately resolved by a single-PFR model assuming uniform axial flow and properties. Consequently, critical transport phenomena such as heat conduction and particle diffusion are poorly represented. Secondly, in a single-PFR framework, the radial temperature profile is inherently flat, rendering it impossible to determine the peak turbulent viscosity from the model itself. As a result, an external prescription of turbulent viscosity, often derived from more detailed multi-PFR simulations, is required, compromising the model's internal consistency. Furthermore, although the energy cost predicted by the single-PFR approach may incidentally align with baseline values when using an externally imposed viscosity, such agreement is likely fortuitous and does not imply genuine predictive capability. Comprehensive validation under varying operating conditions is essential to assess the reliability of this simplified approach. Therefore, we conclude that the single-PFR model lacks both the physical fidelity and general applicability required for accurate modelling of non-uniform plasma conditions, particularly in the context of the present study, where pronounced radial gradients in species concentrations and gas temperature are observed.

The highest energy cost is observed when two PFRs are used in the central region. Then, increasing the number of PFRs in both the central and outer regions results in energy costs that approach the baseline value (*i.e.*, 3.37 MJ(mol N)$^{-1}$ for 32 and 16 PFRs in the central and outer regions, respectively), albeit at the expense of significantly higher computational cost. In comparison, a configuration with 8 and 4 PFRs in the central and outer regions, respectively, reduces computational cost by over 91% while maintaining more than 96% accuracy. This configuration represents the optimal trade-off between accuracy and efficiency in the tested range. Accordingly, except for the first subsection 'Temperature and species distribution analysis' (which uses 32 and 16 PFRs for the central and outer

regions, respectively, to better resolve the spatial distribution of parameters), all subsequent calculations in the munuscript are based on the revised configuration, *i.e.*, 8 and 4 PFRs for the central and outer regions, respectively.

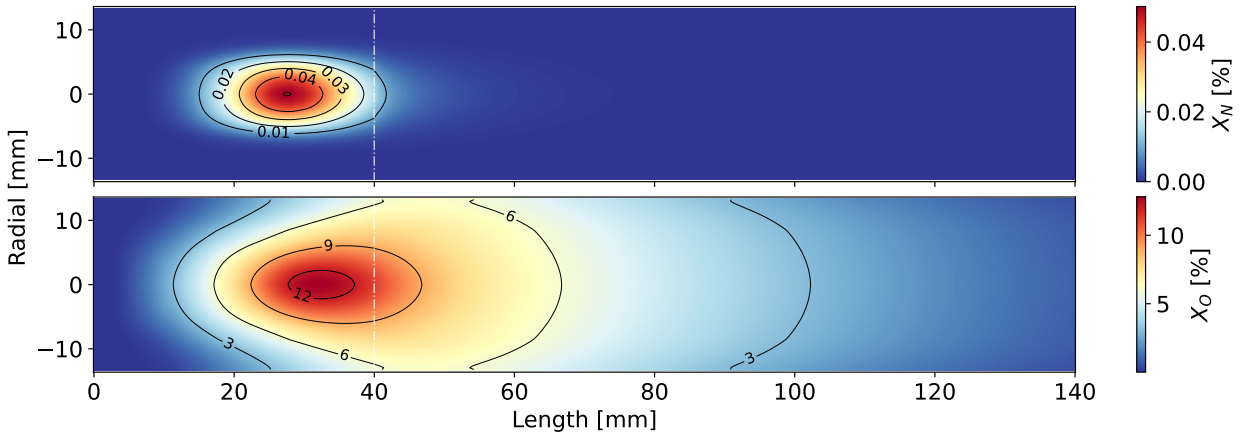

Figure S3: N and O molar fraction distributions in the cross-sectional plane in the middle of the reactor at 50% N_2 fraction. The black dashed line indicates the boundary between discharge and afterglow.

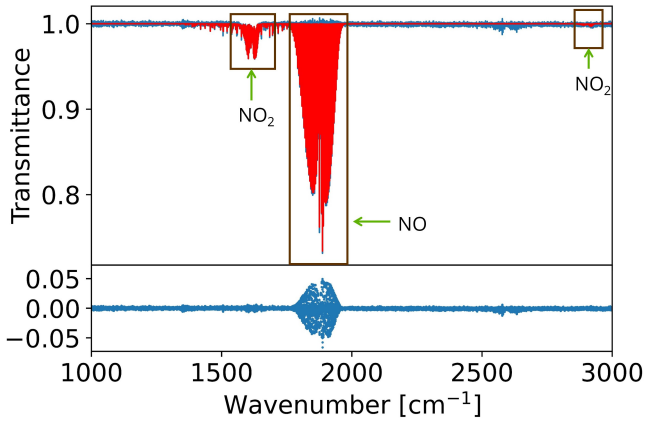

Figure S4: Example of FTIR spectrum fit, indicating which transmittance features belong to which chemical species. The simulated fit, using the HITRAN database,[11] is shown in red, overlapping the blue experimental spectrum. The bottom subplot (also in blue) shows the difference between the fit and the spectrum.

References

(1) Wang, X.; Hong, Q.; Hu, Y.; Sun, Q. On the accuracy of two-temperature models for hypersonic nonequilibrium flow. *Acta Mechanica Sinica* **2023**, *39*, 122193.

(2) Shen, Q.; Pikalev, A.; Gans, J.; Kuijpers, L.; Guerra, V.; van de Sanden, M. C. M. Boosting the NO_x production in microwave air plasma: A synergy of chemistry and vibrational kinetics. *Plasma Sources Science and Technology* **2026**, doi: 10.1088/1361–6595/ae2d91.

(3) Samadi Bahnamiri, O.; Verheyen, C.; Snyders, R.; Bogaerts, A.; Britun, N. Nitrogen fixation in pulsed microwave discharge studied by infrared absorption combined with modelling. *Plasma Sources Science and Technology* **2021**, *30*, 065007.

(4) Wolf, A. J.; Righart, T. W.; Peeters, F. J. J.; Bongers, W.; van de Sanden, M. C. M. Implications of thermo-chemical instability on the contracted modes in CO_2 microwave plasmas. *Plasma Sources Science and Technology* **2020**, *29*, 025005.

(5) Wolf, A. J.; Peeters, F. J. J.; Groen, P.; Bongers, W.; van de Sanden, M. C. M. CO_2 conversion in nonuniform discharges: Disentangling dissociation and recombination mechanisms. *The Journal of Physical Chemistry C* **2020**, *124*, 16806–16819.

(6) Altin, M.; Viegas, P.; Vialetto, L.; van de Steeg, A.; Longo, S.; van Rooij, G.; Diomede, P. Energy partitioning in N_2 microwave discharges: integrated Fokker–Planck approach to vibrational kinetics and comparison with experiments. *Plasma Sources Science and Technology* **2022**, *31*, 104003.

(7) Tatar, M.; Vashisth, V.; Iqbal, M.; Butterworth, T.; van Rooij, G.; Andersson, R. Analysis of a plasma reactor performance for direct nitrogen fixation by use of three-dimensional simulations and experiments. *Chemical Engineering Journal* **2024**, *497*, 154756.

(8) Shen, Q.; Pikalev, A.; Peeters, F.; Guerra, V.; van de Sanden, M. C. M. Pinpointing energy transfer mechanisms in the quenching process of microwave air plasma. *Journal of Physics D: Applied Physics* **2025**, *58*, 275203.

(9) Vervloessem, E.; Aghaei, M.; Jardali, F.; Hafezkhiabani, N.; Bogaerts, A. Plasma-based N_2 fixation into NO_x: insights from modeling toward optimum yields and energy costs in a gliding arc plasmatron. *ACS Sustainable Chemistry & Engineering* **2020**, *8*, 9711–9720.

(10) Viegas, P.; Vialetto, L.; Wolf, A.; Peeters, F. J. J.; Groen, P.; Righart, T.; Bongers, W.; van de Sanden, M. C. M.; Diomede, P. Insight into contraction dynamics of microwave plasmas for CO_2 conversion from plasma chemistry modelling. *Plasma Sources Science and Technology* **2020**, *29*, 105014.

(11) Rothman, L. S.; Gordon, I. E.; Barbe, A.; Benner, D. C.; Bernath, P. F.; Birk, M.; Boudon, V.; Brown, L. R.; Campargue, A.; Champion, J.-P.; others The HITRAN 2008 molecular spectroscopic database. *Journal of Quantitative Spectroscopy and Radiative Transfer* **2009**, *110*, 533–572.